



UNIVERSITY OF LEEDS

This is a repository copy of *Local and Global Granular Mechanical Characteristics of Grain–Structure Interactions*.

White Rose Research Online URL for this paper:  
<http://eprints.whiterose.ac.uk/126329/>

Version: Accepted Version

---

**Article:**

Jahanger, ZK [orcid.org/0000-0003-2869-9178](https://orcid.org/0000-0003-2869-9178), Sujatha, J and Antony, SJ [orcid.org/0000-0003-1761-6306](https://orcid.org/0000-0003-1761-6306) (2018) Local and Global Granular Mechanical Characteristics of Grain–Structure Interactions. *Indian Geotechnical Journal*, 48 (4). pp. 753-767. ISSN 0971-9555

<https://doi.org/10.1007/s40098-018-0295-5>

---

© Indian Geotechnical Society 2018. This is an author produced version of a paper published in *Indian Geotechnical Journal*. Uploaded in accordance with the publisher's self-archiving policy. The final publication is available at Springer via <https://doi.org/10.1007/s40098-018-0295-5>.

**Reuse**

Items deposited in White Rose Research Online are protected by copyright, with all rights reserved unless indicated otherwise. They may be downloaded and/or printed for private study, or other acts as permitted by national copyright laws. The publisher or other rights holders may allow further reproduction and re-use of the full text version. This is indicated by the licence information on the White Rose Research Online record for the item.

**Takedown**

If you consider content in White Rose Research Online to be in breach of UK law, please notify us by emailing [eprints@whiterose.ac.uk](mailto:eprints@whiterose.ac.uk) including the URL of the record and the reason for the withdrawal request.



[eprints@whiterose.ac.uk](mailto:eprints@whiterose.ac.uk)  
<https://eprints.whiterose.ac.uk/>

**Local and global granular mechanical characteristics of grain-structure interactions**

1  
2  
3  
4  
5  
6  
7  
8  
9  
10  
11  
12  
13  
14  
15  
16  
17  
18  
19  
20  
21  
22  
23  
24  
25  
26  
27  
28  
29  
30  
31  
32  
33  
34  
35  
36  
37  
38  
39

## 40 **Abstract**

41 The focus of this work is on systematically understanding the effects of packing density of the sand grains on both  
42 the internal and bulk mechanical properties for strip footing interacting with granular soil. The studies are based  
43 on particle image velocimetry (PIV) method, coupled with a high resolution imaging camera. This provides  
44 valuable new insights on the evolution of slip planes at grain-scale under different fractions of the ultimate load.  
45 Furthermore, the PIV based results are compared with Finite Element Method (FEM) simulations in which the  
46 experimentally characterised parameters and constitutive behaviour are fed as an input, and a good level of  
47 agreements are obtained. The reported results would serve to the practicing engineers, researchers and graduate  
48 students in unravelling the mechanics of granular soil at both local and global levels when they interact with  
49 structures. The outcomes would be beneficial not only to the geotechnical engineering community, but also to  
50 related disciplines dealing with granular materials such as materials processing, minerals and space exploration.

51

52 **Keywords** Granular mechanics, PIV, FEM, bearing capacity, grain-structure interaction

53

## 54 **Introduction**

55

56 Cohesionless sands comprise of discrete grains of varying size and packing density. Their mechanical behaviour  
57 is different from that of conventional solid, liquid and gaseous state of matter [1]. Numerous researchers have  
58 studied the micromechanical characteristics of granular materials using experiments, theoretical descriptions and  
59 computer simulations [2]. From the micromechanical perspective [3], some studies have attributed the origin of  
60 shear strength of granular media to the anisotropy of strong force chains [4-6]. Their dilation characteristics are  
61 attributed to the displacement network of granular media [7].

62 In foundation engineering, ultimate bearing capacity ( $q_{ult}$ ) and allowable settlement ( $S$ ) are used as key design  
63 parameters [8-9]. In sand, settlement controls the design criteria of footing [10-11] which is independent of the  
64 loading rate [9]. Also, the settlement of footings could depend on their width for a given soil [11], but ultimate  
65 bearing capacity of sand is less dependent on footing width ( $B$ ) when less than 1m as reported by Terzaghi and  
66 Peck [12]. In soil-structure interaction analysis [13], engineers use constant vertical displacement profiles for rigid  
67 footings interacting with sand at the level of the footing. However, the settlement in sand could vary significantly  
68 below the level of the footing-sand interface within the influence zone of depth ( $z$ ) about 2-4 times the width of  
69 the footing ( $B$ ) in homogenous sand [14-15]. The previous research discussed above on the settlement profiles

70 along the footing central axis do not vary linearly with depth. However, detailed information on how the  
71 displacement field evolves within the sand bed under mechanical loading is still not well established. Historically,  
72 bi-linear model (simple triangle approximation) is used to describe the variation of elastic displacement in sands  
73 [14] and others use nonlinear variation [16]. At the micro scale, grain displacements are non-uniform [17].  
74 However experimental results on the role of relative density of sand for all three major types, loose, medium-  
75 dense and dense sand on their geomechanical characteristics using particle image velocimetry (PIV) is not yet  
76 probed systematically. This is addressed here using two-dimensional particle image velocimetry (PIV). The  
77 Dynamic Studio Software Platform (DSSP) helps to display the large amounts of PIV-based experimental data in  
78 pictorial forms [18]. Recently PIV was applied to understand the flow properties of granular materials [19]. Here,  
79 the authors focus on the local deformation and velocity fields and bulk strength for different relative densities of  
80 sand when a strip shallow footing interacts with sand under quasi-static axial loading ( $P$ ). Detailed experimental  
81 characterisation of the sand material is made using a range of experiments. The aim is at first to compare the  
82 variation of displacement fields measured in sand packing using PIV with FEM analysis. Thereafter, the variation  
83 of fundamental mechanical features at both local and global scales are studied in detail using PIV for strip footing  
84 interacting with sand packing of different relative densities in a systematic manner.

85

### 86 **Digital Particle Image Velocimetry (DPIV) Analysis**

87

88 DPIV pertains to the digital platform of Particle Image Velocimetry (PIV), is often used in the field of fluid  
89 mechanics to track the motion of fluid flow using tracer particles [20]. It has been also used to study the  
90 displacement and(/or) strain distribution in some cases of granular materials [21-22]. Recently, PIV has been  
91 applied to get measurements of soil deformation in geotechnical engineering problems [21-25]. In this study,  
92 DSSP is used to analyse the digital images acquired during test using PIV. The DSSP platform provides a range  
93 of techniques for characterising particle motions, making it the most convenient for making advanced scientific  
94 imaging-based measurements [18]. The algorithms provided within DSSP are used to analyse the PIV  
95 measurements further. This functionality built in the DSSP was used to analyse the digital frames of the grains,  
96 and to calculate two velocity components vectors of the grains and their evolution during load application within  
97 the sand layer between two successive images. In this study, the area of interest or the target area (full image) was  
98 specified before being divided into sub-sections called interrogation areas (IA) of  $16 \times 16$  pixels each covering a  
99 zone of soil approximately  $2.2 \text{ mm}^2$ . Each of these interrogation area was tracked using an adaptive PIV method

100 [18, 19, 26] to identify the movement of soil based on particle images (here 30 images per second) obtained from  
101 the front of the Perspex test rig. The interrogation areas from each successive images are cross-correlated with  
102 each other, pixel by pixel [18]. The correlation produces a peak signal detection, identifying the common grains  
103 movement and thus also the velocity vector output is computed with sub-pixel interpolation. A velocity vector  
104 plot over field of view (target area) is acquired by repeating the cross-correlation for each interrogation area over  
105 the two images [18].

106

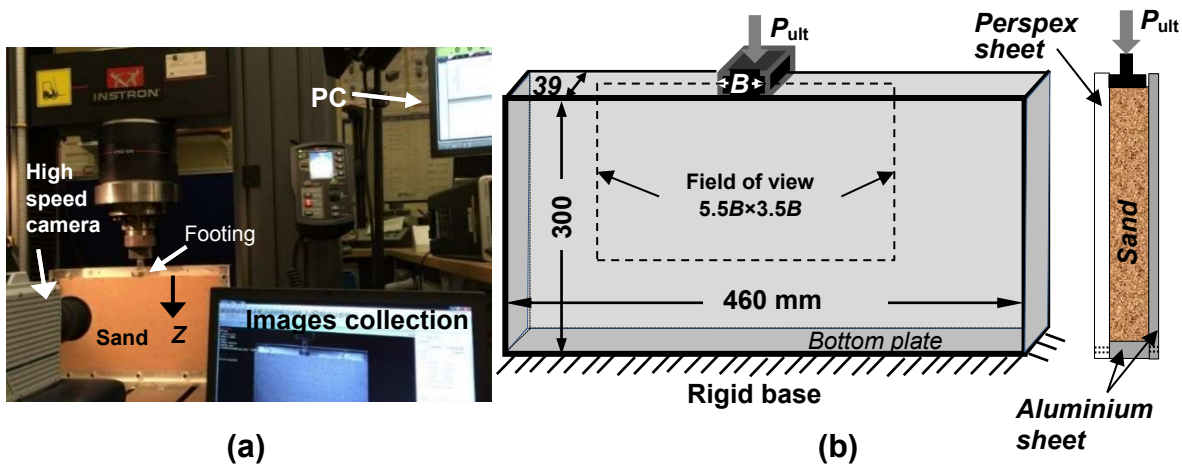
## 107 **Materials and Experiments**

108

109 The samples used here are disturbed dry silica sand samples obtained in UK. Sand properties were characterised  
110 (Table 1) according to the American Society for Testing and Materials [27-28]. Their experimentally measured  
111 material properties and size distribution showed the following properties: maximum dry density ( $\gamma_{d \max.}$ ) =16.50  
112 kN/m<sup>3</sup> and minimum dry density ( $\gamma_{d \min.}$ ) =14.23 kN/m<sup>3</sup>. In addition, using the sieve analysis as shown in Online  
113 Resource OR1, the following properties of sand were obtained from the grain size distribution curve:  $D_{10}$ =0.25  
114 mm;  $D_{30}$ =0.31 mm;  $D_{60}$ =0.40 mm (10%, 30% and 60% of the particles are finer than these particular particle sizes  
115 respectively);  $D_{50}$ = 0.37 (Mean grain size of soil particle); uniformity coefficient  $C_U$ =1.55; and the coefficient of  
116 curvature  $C_C$  =0.93. These data revealed that the soil chosen is a poorly graded sand [17, 29]. The roundness of  
117 the grain was mostly spherical to sub-prismoidal and the angularity of the grains are characterised as angular and  
118 sub-angular [28]. For this, digital microscopy images of the grain samples were used as shown in the Online  
119 Resource OR1.

120 Bearing capacity of the footing was tested using an aluminium box of 460 mm in length, 300 mm in height and  
121 39 mm in thickness, filled with dry silica sand. The box had smooth and transparent Perspex walls of 15 mm  
122 thickness also to eliminate any bending effects during the test (Fig. 1). The authors also verified during all tests  
123 that under the ultimate loads ( $P_{ult}$ ) of the dense sand packing did not lead to any remarkable out of plane movement  
124 of the container's face. This was checked using a dial gauge (0.01 mm resolution) mounted to the side walls from  
125 a magnetic base (though the picture of this arrangement is not included here). The surface roughness of the footing  
126 in contact with sand, and the Perspex walls of the experimental box was measured using 3D optical microscopy  
127 based on white light interferometry [30] from which the mean roughness value  $R_a$  was obtained as 3.204  $\mu$ m and  
128 0.99  $\mu$ m respectively. The rigid foundation base was relatively rough (ratio between the angle of interfacial friction  
129 of the footing ( $\delta$ ) and angle of internal friction of the sand ( $\phi$ ), ( $\delta / \phi$ ) is 0.25). Two cases of footing width are

130 considered in this study, i.e., smaller and larger footing width with dimensions  $38 \times 38 \times 15 \text{ mm}^3$  and  $76 \times 38 \times$   
 131  $15 \text{ mm}^3$  respectively (footing width  $B/D_{50} = 102$  and  $204$  respectively to avoid any grain size effect, and  
 132 height=15 mm) was used here. It is recognised that the scale effects of the footing model could affect the  
 133 estimations of their strength characteristics [31]. For example, a footing with relatively small width would require  
 134 a relatively low stress level in the laboratory experiments, as if it were on a denser “state” of soil than a larger  
 135 footing, even if they were tested on sand with the same void ratio [31]. To minimize the scaling effect, it is  
 136 suggested that the model testing for studying the effect of packing density should not be too close to the limits of  
 137 void ratio ( $e_{\max}$  and  $e_{\min}$ , [32]). Taking this into account in the present study, the packing densities are kept away  
 138 from these limits (Table 1). The value of  $B/D_{50}$  used here is within the permissible limit of testing strip footing in  
 139 the lab although footing sizes used in real practice could be higher [33]. Such model dimensions have been used  
 140 in previous experimental studies in this field [8, 34]. To minimise any frictional effects of the footing with the  
 141 wall, a small gap of 1 mm is allowed between the footing and the back wall, so that they do not affect the  
 142 deformation of the soil recorded by PIV at the front of the box. It is also worth noting that about 12.5% of particles  
 143 were in the size range of 0.5-0.9 mm as shown in the Online Resource OR1, which helped to avoid any noticeable  
 144 leakage of grains from behind the footing. These measures ensure that the observed movement from the images  
 145 is due to the inner movement in the grains under mechanical loading [30].



146  
 147 **Fig. 1** (a) Experimental setup using PIV with a live image of footing in contact with sand (b) schematic diagram  
 148 of the experimental setup (dimensions are in mm)

149  
 150 The degree of compaction of granular soil is normally characterised according to the relative density  $D_r$ , defined  
 151 as [35]:

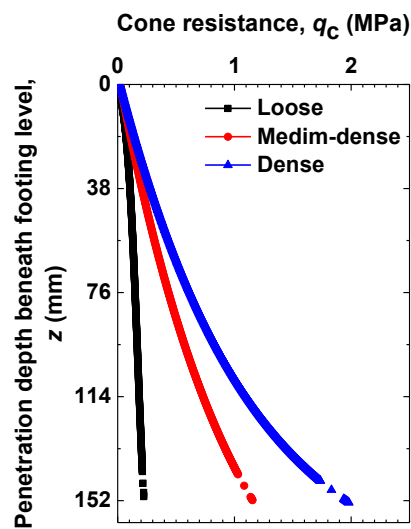
152 
$$D_r(\%) = \frac{e_{\max} - e}{e_{\max} - e_{\min}} \times 100 \quad (1)$$

153 Where  $e_{\max}$  and  $e_{\min}$  are void ratio of the soil in loosest and densest conditions respectively and  $e$  is in-place void  
154 ratio of the tested soil (Table 1). Three cases of relative densities ( $D_r$ ) loose (L), medium-dense (M) and dense  
155 (D) were used in this study. The loose granular packing ( $\gamma=14.7$  kN/m<sup>3</sup>,  $D_r=24 \pm 2\%$ ,  $e=0.76$ ) was prepared by  
156 pouring the grains mass uniformly across the width of the box in small layers using pluviation technique method  
157 [36] so that any segregation of the grains was avoided during the construction process. The top surface of the sand  
158 layer was gently levelled off using a hand scraper. This researchers also took care not to disturb the constructed  
159 loose sample in any way before applying the axial loading in our experiments. The mass of sand grains laid in  
160 the box to the required height pertains to the density of the loose sample. The medium-dense packing ( $\gamma=15.30$   
161 kN/m<sup>3</sup>,  $D_r=53 \pm 2\%$ ,  $e=0.7$ ) was hand compacted in three layers, using 50 blows per layer in 0.035 m lifts each  
162 with a 16 cm<sup>2</sup> compaction hammer of 0.92 kg weight designed for this purpose [31]. The dense sand ( $\gamma=15.80$   
163 kN/m<sup>3</sup>,  $D_r=72 \pm 2\%$ ,  $e=0.64$ ) was achieved in five layers, 60 blows per layer. The footing was placed  
164 symmetrically on the top surface of the sand bed.

165 An axial compression loading ( $q$ ) was applied slowly on the footing (0.05 mm/s penetration velocity) using an  
166 Instron loading machine with 0.1N resolution (Fig. 1). The loading machine also had an inbuilt dial gauge (linear  
167 variable differential transformer, LVDT) to record the vertical displacement of the indenting footing on the sand  
168 packing. The macroscopic load and vertical displacement of the footing were also measured from the tests. The  
169 PIV camera with an allowable frame speed up to 100000 frames per second (fps) was fixed in front of the box  
170 and two light sources were used to illuminate the rig. However, as the loading condition is quasi-static in this  
171 study, the recording at 30 fps was found to be adequate until soil failure was reached, although higher frame  
172 speeds were considered in the early stages of the experimental programme. We had verified that the recording at  
173 greater than 30 fps did not affect the result noticeably. The resolution of the images was  $1920 \times 1080$  pixels.  
174 Initially, a number of trials were conducted to determine the suitable acquisition rate of the recorded PIV images  
175 for the analysis. It was found that, for the current experiments, an acquisition of 1 frame/s of the recorded images  
176 is adequate in which images were captured at displacement increments of 0.0017 mm. DSSP was used to analyse  
177 the images using an adaptive PIV [18]. The adaptive PIV iteratively adjust the size of the individual interrogation  
178 areas (IA) in order to adapt to local seeding densities and flow gradients [18]. This is suitable to study granular  
179 systems even under different flow conditions [19] and bearing capacity of layered system [26]. Here, the  
180 distribution of velocity vectors of the grains was examined in the image analysis using a minimum interrogation  
181 area (IA) of size  $16 \times 16$  pixels and maximum IA size of  $64 \times 64$  with a measurement resolution of sub-pixel [18].  
182 The space-pixel dimension of the measurement was calibrated by printing a known scale on the test box along the

183 horizontal and vertical directions. White et al. [24] have shown that the precision of the measurement (i.e., the  
 184 random difference between multiple measurements of the same quantity) improves with larger PIV patches and it  
 185 is inversely proportional to the amount of the measurement resolution. This size of the mesh patch used here  
 186 reveals a standard error better than 0.01 pixel [18, 24]. In the experiments, two illumination lights were positioned  
 187 above the testing box to avoid reflection and glare on the measurement side of the Perspex wall. It was verified  
 188 that the variation in image scale in both horizontal and vertical direction were not significantly different. The PIV  
 189 camera lens was focused normal to plane the footing-soil interface region where the measurements are most  
 190 important to make. Therefore, the dimension of target area was  $\sim 5.5B \times 3.5B$  (Fig.1). The displacement measures  
 191 i.e. resultant displacement ( $S_R$ ), vertical displacement ( $S_v$ ) and horizontal displacement ( $S_h$ ) were evaluated under  
 192 a given load in total (i.e., between the reference image at zero load ( $q=0$ ) and the image at the required fractions  
 193 of the ultimate load level, such as  $0.34q_{ult}$  and  $q_{ult}$ . A typical mean size of sand grain ( $D_{50} = 0.37$  mm) was  
 194 represented by about  $3 \times 3$  pixels. Hence the PIV experimental measurements made here are at the local-scale.

195 Following the footing tests, two standard cone penetration test (CPTs) tests were also conducted for each soil  
 196 density to characterise the samples using a 10 mm diameter model CPT [25, 29]. The CPT was inserted at a  
 197 penetration rate of 1 mm/s in the current experiments as shown in Online Resource OR2, but using the identical  
 198 filling procedure of the grains used in the footing–sand indentation experiments presented earlier. Figure 2 shows  
 199 the CPT penetration profiles for the soil for all sand packings. The penetration resistance (Cone resistance =  $q_c$ )  
 200 profiles are plotted against the penetration depth from the bottom level of the footing.



201

202

Fig. 2 CPT data for the sand packing

203 As expected, the penetration resistance of dense sand is higher than medium-dense and loose sand. The penetration  
204 resistance of loose sand remains almost constant with depth after  $z/B = 2.5$ , but penetration resistance for medium-  
205 dense and dense sand increase with depth at an increasing rate. The rate of the penetration resistance of dense  
206 sand is larger than that of the medium-dense. Again, the differences in the penetration resistance for different  
207 relative densities are primarily accounted for the relatively larger volumetric compressibility in loose, medium-  
208 dense sand than the dense sand. The CPTs results for all the densities show the average response of the two results  
209 (error within 5%).

210

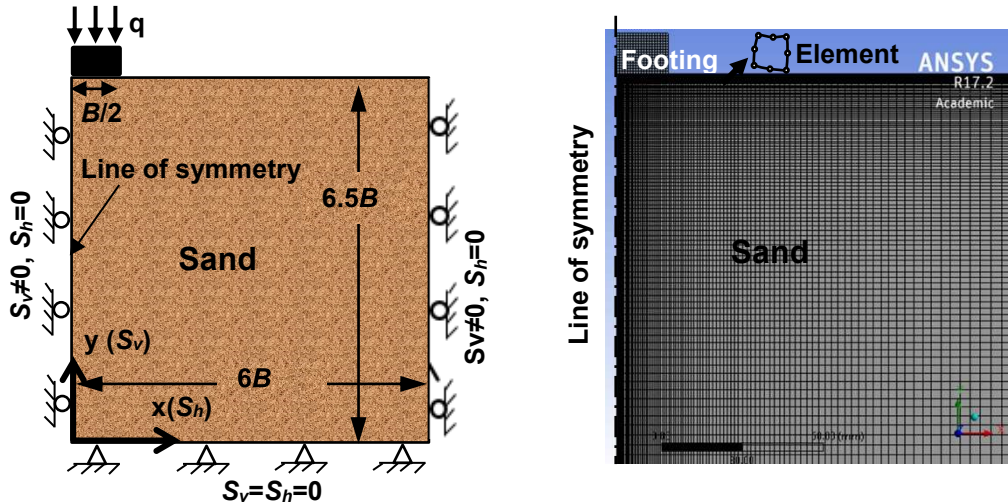
## 211 **FEM Simulations**

212

213 Non-linear elastic finite element simulations have been made for the cases of a single footing indenting on the  
214 loose, medium-dense and dense sand packing using ANSYS workbench 17.2 version [37]. The ANSYS program  
215 is a broad purpose finite element modelling (FEM) package for numerically solving a wide variety of mechanical  
216 interactions [37].

217 In the present study, ANSYS is used to create a two-dimensional solid geometry. The chosen domain along with  
218 applied boundary conditions is shown in Fig. 3. The simulations were held under identical boundary conditions  
219 for footing indenting with different types of sand packing as in the case of physical experiments. In the  
220 simulations, the bottom most nodes were fully constrained in both the horizontal and vertical directions ( $S_v = S_h$   
221  $= 0$ ). A line of symmetry is used along the footing centre line ( $S_v \neq 0, S_h = 0$ ). The far side of the assembly was  
222 fully constrained in the horizontal direction ( $S_h = 0$ ) and free to move in the vertical direction ( $S_v \neq 0$ ) [38-39]. The  
223 contact regions between the rigid footing and the sand were modelled as a relatively rough surface (interface  
224 friction coefficient=0.25) corresponding to the experimental study [40]. An adaptive FE mesh was generated at  
225 the footing-soil interface where the largest stresses and strains would be expected. It should be mentioned that  
226 Skewness mesh metric (a measure of mesh quality) of 0.132 maximum value was obtained which is acceptable  
227 [41]. The size of the elemental geometry is shown in Fig. 3. The nodes and element numbers in the soil body are  
228 equal to 44000 and 14360 respectively.

229 Material model for soil describes the nonlinear plasticity behaviour which depends on the engineering soil  
230 properties in the current ANSYS simulations. For this, the experimentally characterised bulk stress-strain  
231 relationship corresponding to the load-displacement curves of different packing densities presented in Figure 4  
232 are discretised into a large number of linear segments and fed as user defined digital input [37, 41].



233

234

235 **Fig. 3** (left) Chosen domain and boundary conditions, half of domain analysis not to scale (right) finite element  
 236 mesh, and element enlarged.  $S_v$  is vertical displacement component and  $S_h$  is horizontal displacement component.  
 237  $B$  is the footing width

238

239 Furthermore, the experimentally characterised material physical properties were used i.e. bulk density, initial  
 240 modulus of elasticity ( $E$ ) and typical value of Poisson's ratio ( $\nu$ ) for sand ( $E = 25$  MPa, 35 MPa and 50 MPa  
 241 whereas  $\nu = 0.2, 0.25$  and  $0.35$  for the loose, medium-dense and dense sands respectively [11]). In the present  
 242 analysis, ANSYS used the multilinear isotropic hardening of the stress-strain relation [41]. The width of the  
 243 loading area is  $0.5B$ . The loading is applied vertically in increments of constant displacement of  $0.15B$ , uniformly  
 244 across the width of the footing within the time step of 0.01 second (~300 cumulative iteration). The evolution of  
 245 different displacement components in the solid geometry (depicting the sand packing) is tracked for different  
 246 loading levels and compared with corresponding PIV measures later.

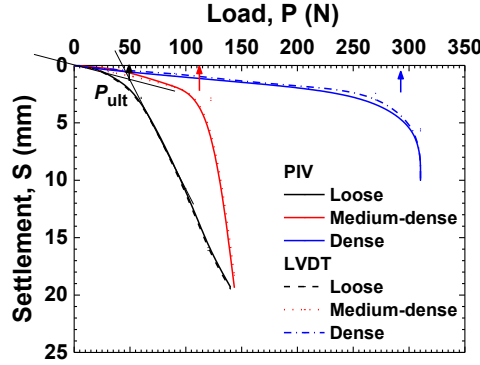
247

## 248 Results and Discussions

249

250 The load–settlement relationship for a typical footing ( $B = 38$  mm) interacting with sand is presented in Fig. 4. It is  
 251 worth mentioning that these PIV curves loads are simultaneously measured using the corresponding load outputs  
 252 from the Instron. The settlements obtained using the PIV and LVDT gauge agree well. This justifies applying PIV  
 253 to examine the displacement measures in sand layer later. Using the load-settlement data, the tangent intersection  
 254 method [42] was applied to obtain the value of the ultimate bearing capacity (Fig. 4). The ratio of ultimate vertical  
 255 settlement under ultimate load ( $S_u$ ) to footing breadth ( $B$ ),  $S_u/B$  is  $\sim 5.0, 7.1$  and  $11.7$  % for the loose, medium-

256 dense and dense sand respectively. These measures and the nature of bulk load-settlement curves are consistent  
 257 [11] with punching (without a well-defined peak), local shear failure (moderate peak) and general shear failure  
 258 (well-defined peak) for sand described by Liu and Iskander [17], Dijkstra et al. [29], Vesic [43].



259

260 **Fig. 4** Load-settlement curves of footing ( $B=38\text{mm}$ ) interacting with loose, medium-dense and dense sand. The  
 261 guide arrows show the ultimate load level ( $P_{ult}$ ) of the sand packing  
 262

263 Though not presented here, we also obtained a good level of comparison with De Beer's study [44] for the  
 264 variation of  $N_\gamma$  (Bearing capacity factor) with  $\gamma B$  for different sand packing. Both the bearing pressure and the  
 265 failure strain increase with the packing density of sand. The authors wish to point out that, in the case of strip  
 266 footings used in practice, 3D condition could exist around the ends of the strip footings even if the footing is long.  
 267 However, for most parts of long strip footings, plane-strain condition could exist [8, 25, 30] as assumed in the  
 268 current 2D plane-strain experiments [34].

269 The peak angle of internal resistance ( $\phi_{peak}$ ) for all cases of the packing density was also determined from triaxial  
 270 compression test at different confining pressures 100, 200, and 300 kPa. For sands, the angle of internal friction  
 271 typically ranges from  $26^\circ$  to  $45^\circ$ , increasing with the relative density. Three cases of relative densities were used  
 272 as that in the experiment tests: loose, medium-dense and dense. The height of the sand samples was typically 76  
 273 mm, and the diameter was 38 mm. Subsequently, the plots of deviator stress ( $\sigma_d$ ) against axial strain ( $\epsilon_a$ ) were  
 274 made. The peak angle of friction of the soil is obtained according to the stress state at peak strength. The measured  
 275 angles of internal friction are  $32^\circ$ ,  $39.5^\circ$ , and  $44.3^\circ$  for loose, medium-dense and dense sand respectively. Using  
 276 these, the peak angle of shearing resistance of the samples was evaluated and plotted against the relative density.  
 277 This variation is described in (2) as:

278 
$$\phi_{peak} = 24.7 + 0.267 D_r \quad (2)$$

279 Also the ( $\phi_{peak}$ ) determined from the standard direct shear test (ASTM D3080) under three different normal stresses  
280 50, 100 and 200 kPa. The peak angle of shearing resistance of the samples was evaluated and plotted against the  
281 relative density. This variation is described in a mathematical form in (3) as follows:

$$282 \quad \phi_{peak} = 25.2 + 0.277 D_r \quad (3)$$

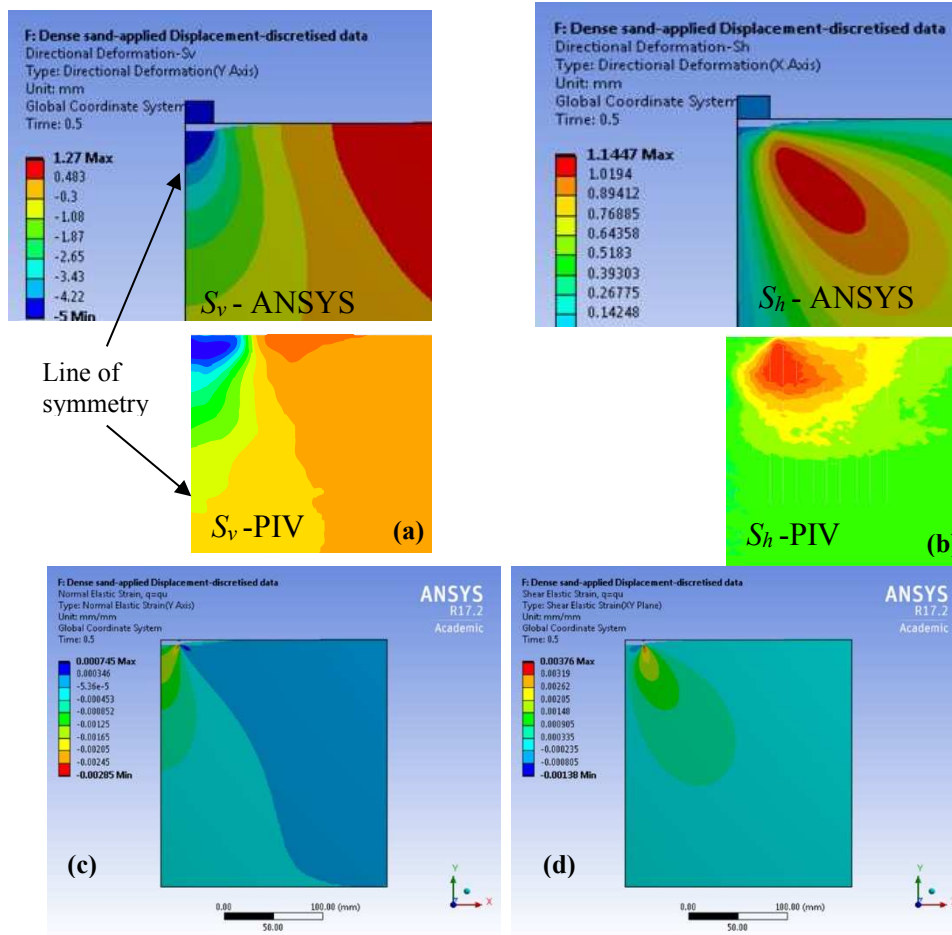
283 This macroscopic relations obtained from the above said characterisation experiments are in agreement with other  
284 literature [8]. The authors wish to point out that, some literature suggest that the shear friction angle measured  
285 using direct shear tests may not pertain to that of sand under the plane strain experiments [36]. Jewell [45]  
286 suggested that symmetrical direct shear test could provide a more reliable measure of the plane strain angle of  
287 friction and the angle of dilation for sand than conventional direct shear test. In some studies, the angle of internal  
288 friction of sand obtained from the conventional direct shear test also correlated well with the experimental results  
289 of plane-strain condition [46]. However, in analysing the footing-soil interactions using theoretical and  
290 computational methods by idealising soil as an elastic media [47], friction angle does not form as a direct input in  
291 the analysis.

292

### 293 **Comparison of the PIV measurements with FEM analysis**

294

295 Here the typical results are presented below for the case of footing interacting with the dense sand packing. Figure  
296 5(a, b) shows the variation of PIV-based vertical displacement component and horizontal displacement component  
297 profiles in the dense sand at ultimate load and compared with the FEM (ANSYS) analysis. It is evident that a  
298 good level of agreement between the PIV and FEM approaches are obtained both qualitatively and quantitatively  
299 up to  $2.5B$  from the footing edges. Furthermore, quantitative comparison of variation of the normalised vertical  
300 displacement component  $S_v$  and the normalised horizontal displacement component  $S_h$  along a horizontal section  
301 at a depth of  $0.5B$  below the level of footing under the ultimate load is provided for different packing conditions  
302 of sand in the Online Resource OR3. A good level of agreement is obtained between them. Figure 5(c, d) shows  
303 the variation of normal and shear elastic strain contours at ultimate load for the case of dense sand using FEM. It  
304 can be seen from the normal and shear elastic strain map that there is a strain concentration around the corner of  
305 the footing. It can be noticed from the contours of shear strain in the dense media that the soil is sheared in the  
306 area below the edge of the footing. Though not presented here, similar observations were made for the loose and  
307 medium-dense sand packing used in this study.



308

309

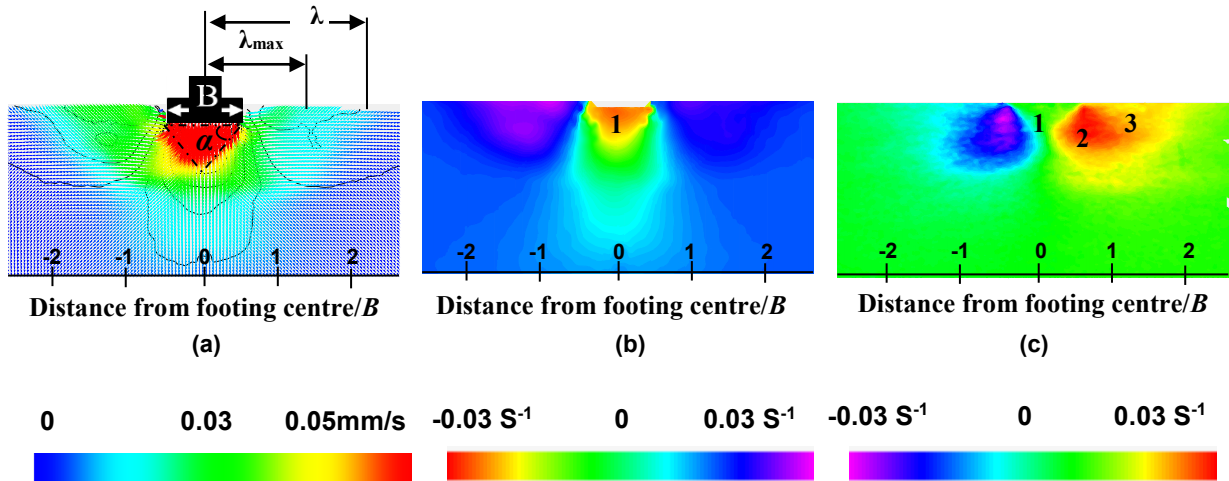
310 **Fig. 5** Comparison of PIV-based vertical displacement profile in dense sand at ultimate load below the footing  
 311 with FEM analysis (identical colour codes are used): (a) vertical displacement component (b) horizontal  
 312 displacement component below the footing. Taking advantage of FEM, the strain distributions are presented: (c)  
 313 normal and (d) shear elastic strain

314

### 315 PIV based analysis of footing-sand interactions

316

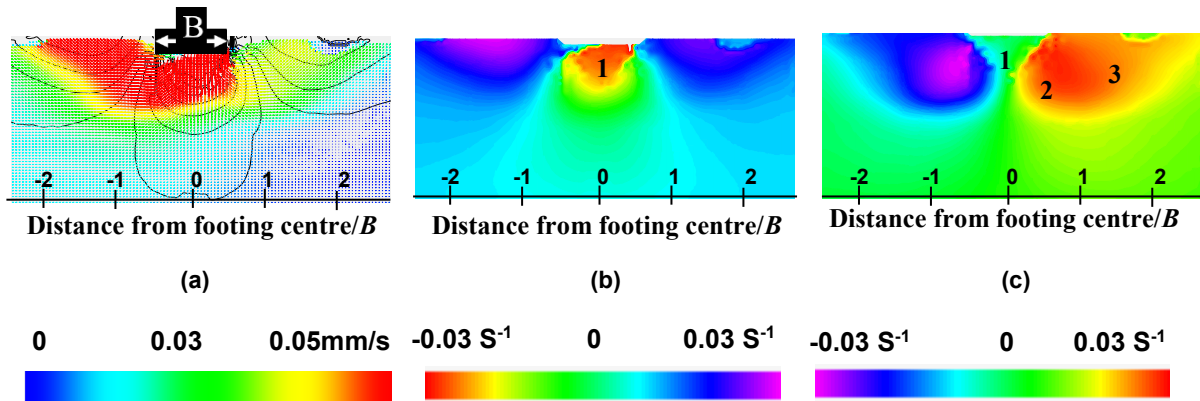
317 Figures 6-8 present typically the evolution of resultant velocity vectors in the sand packing under a typical load  
 318 of  $q=q_{ult}$  ( $B=38\text{mm}$ ). Also the corresponding evolution of vertical and horizontal strain rate ( $\epsilon_v$  and  $\epsilon_h$   
 319 respectively) in the sand packing are provided which help to identify the difference regions of granular flow in  
 320 the sand packing such as dead, active and passive zones as discussed below. The authors had also verified that  
 321 these generic observations were similar in the case of the larger footing width ( $B=76\text{mm}$ ). A detailed evolution  
 322 of this for three more stages of loading is provided in the Online Resource OR4-OR6. In this plot the contours of  
 323 the vertical velocity are also obtained from the DSSP and superimposed for information.



324

325 **Fig. 6** (a) Resultant velocity vectors at a typical load of  $q=q_{ult}$  in loose sand and the scalar contours of the vertical  
 326 velocity using PIV (b) vertical strain rate  $\epsilon_v$  (c) horizontal strain rate  $\epsilon_h$ . Zones: 1- dead zone, 2- active zone, 3-  
 327 passive zone.  $B= 38$  mm

328

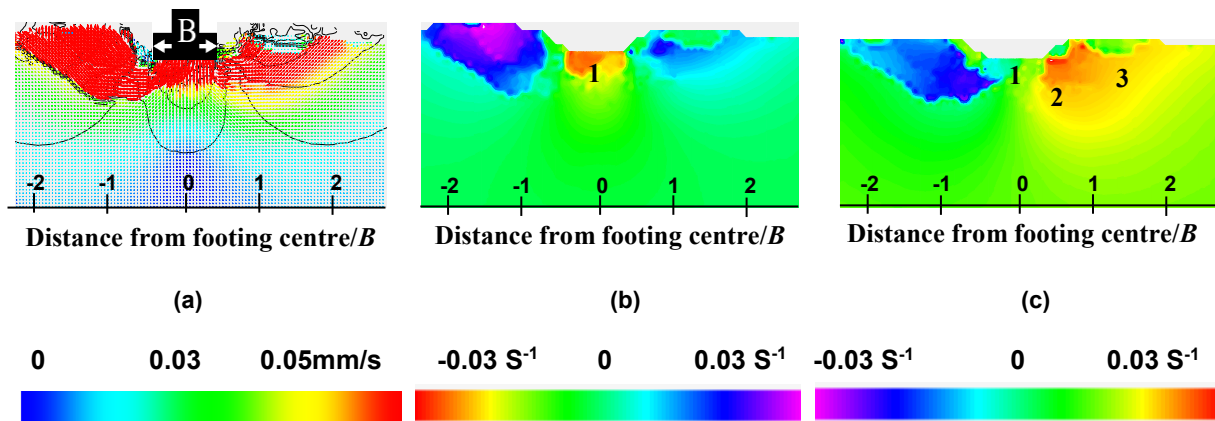


329

330

331 **Fig. 7** (a) Resultant velocity vectors at a typical load of  $q=q_{ult}$  in medium-dense sand and the scalar contours of the  
 332 vertical velocity using PIV (b) vertical strain rate  $\epsilon_v$  (c) horizontal strain rate  $\epsilon_h$ . Zones: 1- dead zone, 2-  
 333 active zone, 3- passive zone.  $B= 38$  mm

334



335

336 **Fig. 8** (a) Resultant velocity vectors at a typical load of  $q=q_{ult}$  in dense sand and the scalar contours of the  
 337 vertical velocity using PIV (b) vertical strain rate  $\epsilon_v$  (c) horizontal strain rate  $\epsilon_h$ . Zones: 1- dead zone, 2-  
 338 active zone, 3- passive zone.  $B= 38$  mm

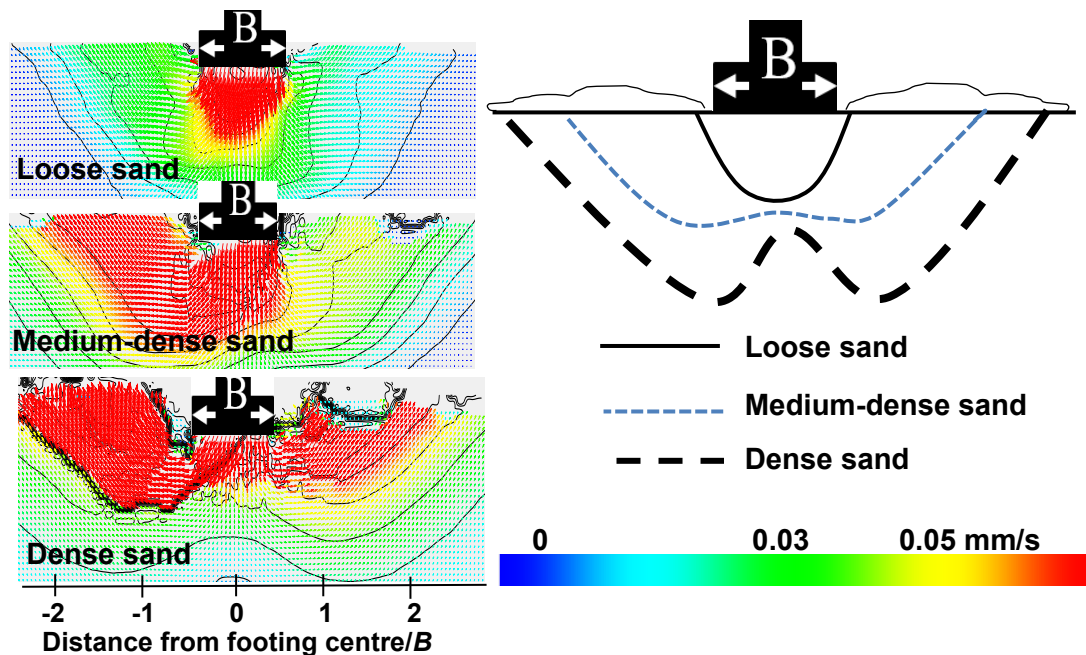
339 At the early stages of the loading (c.a.  $q < 0.5q_{ult}$ ), approximately a triangular wedge of dead zone (region 1 in Figs.  
340 6-8 with a constant amount of resultant velocity of the grains but has the highest vertical velocity) is formed  
341 beneath the footing in all cases of packing densities [48]. The authors point out that the dead zone does not mean  
342 that the grains are not moving at all, but move as a block of grains with almost the same velocity. In granular  
343 mechanics, the dead-zone is characterised by the block of materials beneath the indenting objects with the granular  
344 materials, and moving as if they are continuous extension of the indenter, i.e., no slip at the indenter-granular  
345 interface [22]. Noticeably, outside this zone the particles tended to move downward and sideward symmetrically  
346 until the ultimate bearing capacity is reached in the sand packing. Similar trends were noticed in other studies, for  
347 example in sand [22], different soil types [48] and soft metal [49].

348 The depth of this wedge at the ultimate bearing load is equal to about  $B$ , whose vertices (slip planes) intersect the  
349 horizontal at an angle ( $\alpha =$  Angle of dead zone wedge/active zone 1) of about  $62^\circ \pm 2^\circ$ . These are consistent with  
350 Prandtl's assumption [48] for smooth footing ( $\alpha = 45 + \phi/2$ ), which have not been confirmed using microscopic  
351 experiments, but using PIV here. Furthermore, Kumar and Kouzer [38] have reported similar measures for smooth  
352 footing using plasticity limit analysis with the help of finite element method (FEM). For a further increase in the  
353 load, the grains in the dead zone tend to punch the neighbouring grains in zone 2 radially outwards (Figs.6-8). A  
354 failure pattern consistent with Vesic [43] at the ultimate failure load is visualised (Figs. 6-8, and as in Online  
355 Resource OR4-OR6) for all cases of sand considered here. By and large, the grains flow symmetrically with  
356 respect to the central axis of the footing until reaching the ultimate load ( $q=q_{ult}$ ) then, unsymmetrical flows occur  
357 beyond the ultimate load. This is consistent with the classical literature, e.g. Vesic [43] for medium and dense  
358 sand, but the current study observes that this could happen in the case of loose sand as well. At ultimate load, the  
359 dense soil failed suddenly corresponding to the pronounced peak in the bulk strength curve presented in Fig.4,  
360 and the unsymmetrically strong velocity distribution presented in Fig. 8 at the localised level. So, in the higher  
361 relative density tests, the horizontal displacement (Fig. 8c) seems to be highly non-symmetric under ultimate load.  
362 In reality local structural non-homogeneities could exist, and this triggers the non-symmetrical flow of grain (post-  
363 failure) even under the symmetric loading conditions. At this stage, the grains flow like a fluid. The grains beneath  
364 this flow region are solid-like and almost stagnant. The shear failure occurs progressively from the dead zone and  
365 extending radially outwards.

366 The sand surface forms a heap spreading up to about  $2.7B$ ,  $2.6B$  and  $2.4B$  away from the footing centre ( $\lambda =$   
367 Distance of sand heap from the centre of the footing, Fig. 6) for the loose, medium-dense and dense packing  
368 respectively (Figs. 6-8). The height of the heap attains maximum at distances of about  $1.7B$ ,  $1.55B$  and  $1.31B$  for

369 loose, medium and dense sand respectively ( $\lambda_{max}$ = Location of sand heap attaining maximum height from the  
 370 centre of the footing). The slope of sand heap at the ultimate load is  $31^\circ$ ,  $33^\circ$  and  $38^\circ$  for the loose, medium-dense  
 371 and dense sand respectively. The average value of the slop of the heap for the different sand packing is ( $34^\circ$ )  
 372 identical to the angle of repose of the sand. These angles are close to the residual angle of internal friction of the  
 373 sand ( $\phi_{cr}$ ) about  $31^\circ$ ,  $33^\circ$ ,  $37^\circ$  for the loose, medium-dense and dense sand samples respectively. These residual  
 374 angles are consistent with the previous literature [50].

375 The effect of sand packings at ultimate load on the failure mechanism are summarised both quantitatively and  
 376 systematically in Fig. 9 for a typical case of footing ( $B=38\text{mm}$ ). This shows the resultant velocity vectors of soil  
 377 movement at ultimate bearing capacity and the schematic diagram of the failure mechanism underneath the footing  
 378 of different packing densities. It is evident that the footing load test in the loose packing corresponds to a punching  
 379 failure and local shear mechanism, consistent with the literature [29]. On the other hand, tests in the medium-  
 380 dense and dense packings exhibit a general failure mode with relatively larger horizontal displacement and soil  
 381 heap next to the footing, typical of a conventional rigid plastic bearing capacity, and Prandtl's wedge-shaped zone  
 382 mechanism [48]. Hence, the formations of velocity discontinuities are linked to the density of the sand packing.

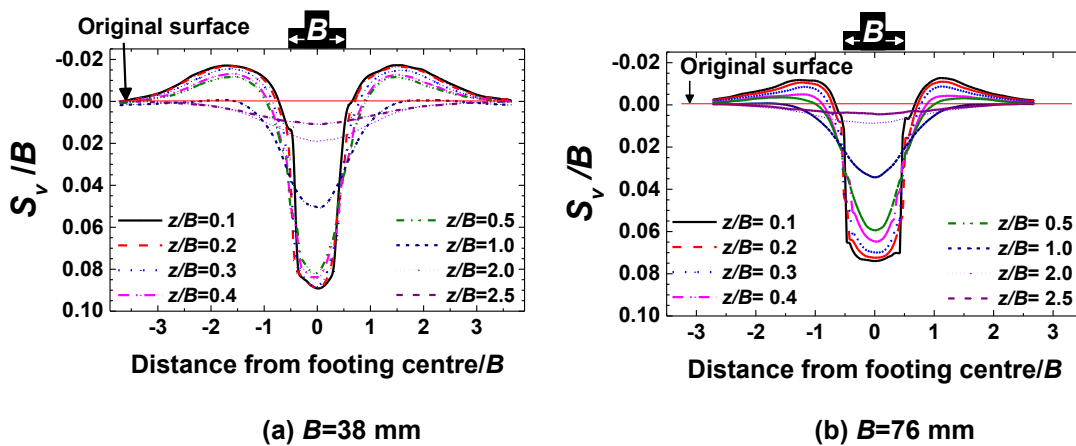


383  
 384 **Fig. 9** (left) Resultant velocity vectors of soil movement under ultimate bearing capacity,  $B=38$  mm (right) sketch  
 385 of general schematic failure mechanism underneath footing of different packing densities  
 386

387 Interestingly, the boundaries of the zone of plastic flow in sand at failure load sketched using PIV here (in terms  
 388 of the resultant velocity vector, and the components of strain rate presented in Figs.6-8) are remarkably similar to

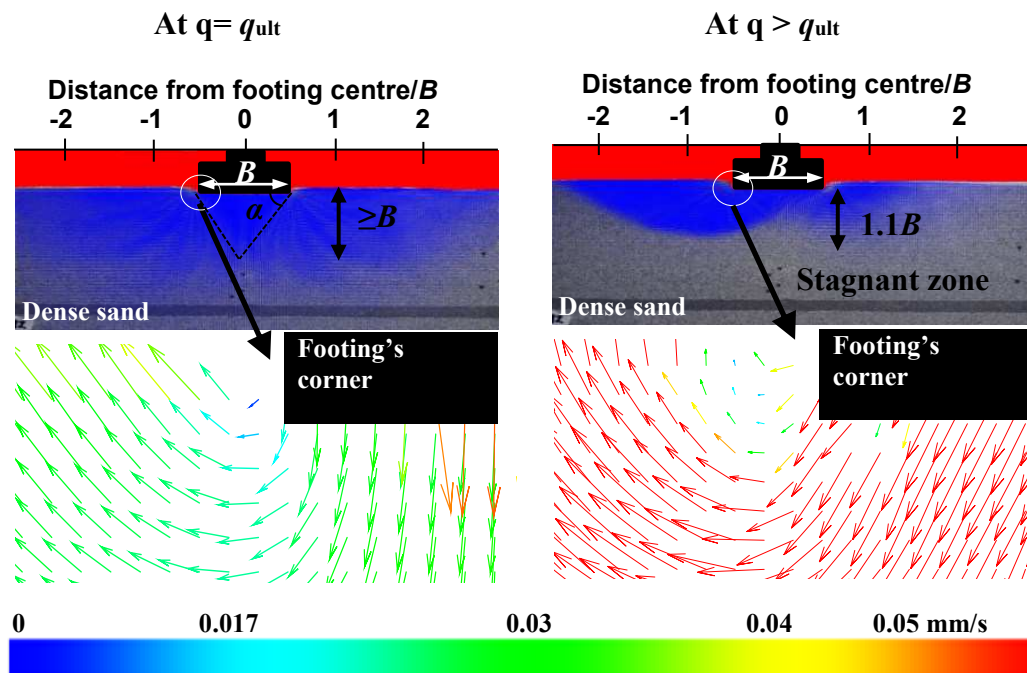
389 such intuitive diagrams suggested by Fröhlich in the 1930's [48]. However, at or beyond the ultimate load, the  
 390 PIV experiments have shown non-symmetric flow of grains even under the symmetric loading conditions on the  
 391 footing. They could be attributed to the potential existence of (even minor level) non-symmetrical structural  
 392 arrangements of the grains at local scale in reality. These could amplify the non-symmetrical velocity patterns  
 393 under the above said condition.

394 Figure 10 shows the typical normalised vertical displacement component in dense sand at different horizontal  
 395 sections below the footing-soil interface under the ultimate load ( $q_{ult}$ ). The plots of this for loose and medium-  
 396 dense sand are provided in the Online Resources OR7. It is evident that at a depth of  $z/B=2.5$  the vertical  
 397 displacement is practically negligible in all cases of footing width and packing densities. Furthermore, for a given  
 398 packing density, the normalised vertical displacement in the soil at a given depth (e.g.  $z/B= 0.1$ ) decreases for an  
 399 increase in the width of the footing under the ultimate load. However, here it is found that the absolute value of  
 400 the vertical displacement in the soil for a given depth increases for increase in the width of the footing as also  
 401 referred in other studies [51]. The heap close to the free surface (secondary peaks) increases with increasing  
 402 relative density but decreases with  $z/B$  (Fig. 10). Also, the heap height decreases with footing width as shown in  
 403 Online Resource OR7. This is related to potentially particles interlocking and rolling over of the grains. This has  
 404 a significant effect in the development of the vortex map adjoining the footing sides [22]. The discontinuities in  
 405 the velocity measures directly beneath the footing and the edges of the footing could result some error in the  
 406 measurement [25]. However, these measurements are taken at and beyond a depth  $z/B= 0.1$  after the ultimate  
 407 loading is applied. Therefore, any such potential errors are expected to be minimal here.



408  
 409 **Fig. 10** PIV-based normalised vertical displacement component profiles in dense sand under the ultimate load  
 410 ( $q=q_{ult}$ ) along different horizontal sections at different depths ( $z/B$ ) from the footing-soil interface  
 411  
 412

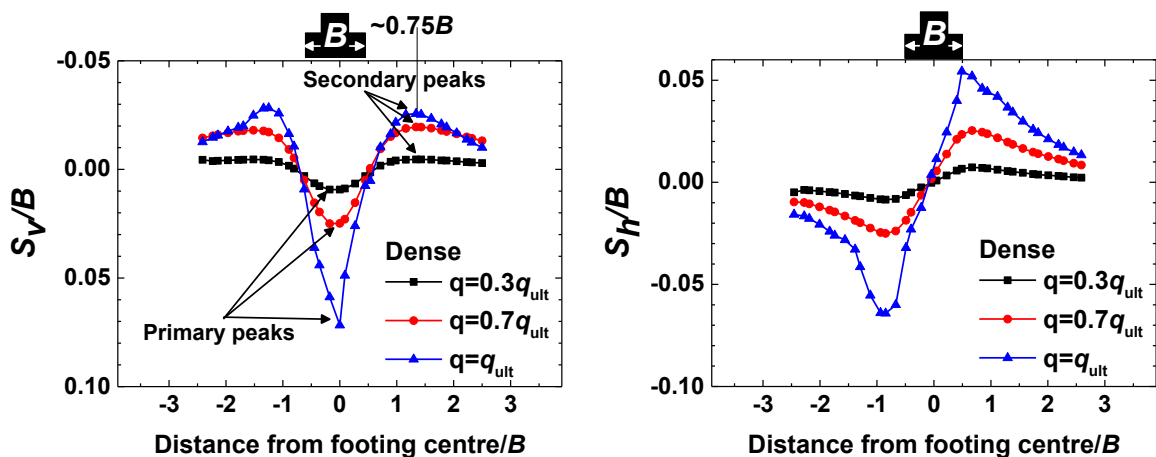
413 The images of flow of grains near the corner of the footing ( $B=38$  mm) for a typical case of dense sand is  
 414 superimposed on their resultant velocity distribution plots and presented in Fig.11 for the pre-failure and post-  
 415 failure stages. These plots for the cases of loose and medium-dense sand are provided in the Online Resource  
 416 OR8. The grains flow radially outwards and non-uniformly in all cases of the sand packing. The grains resting  
 417 beyond the influence zone of deformation (or velocity) do not move in the post-failure stage, which is beyond  
 418 about  $1.25B$ ,  $1.2B$ , and  $1.1B$  for loose, medium-dense and dense sand respectively for both cases of footing width.  
 419 This trend is in agreement with Liu and Iskander [17] who stated that this influence zone is limited within a depth  
 420 of about  $1B$  of the footing at post-failure stage in the case of loose sand ( $D_r$  is limited to 21% in their experiments).  
 421 From the PIV results, the authors observe that the depth of this influence zone is lower than that of pre-failure  
 422 stages possibly due to relatively radially outwards movement from the edge of footing as a block, which is  
 423 consistent with conventional Terzaghi's bearing capacity analysis (Fig.11) [48]. The vortex in the total velocity  
 424 distribution profiles is clearly seen nearer the corner side of the footing for all sand densities. It started when the  
 425 vertical displacement ( $S_v$ ) ratio  $S_v/B \sim 0.1$ . This is a result of gravitational movement of sand from the surface heap  
 426 while the subsurface grains move upward with loading. Eventually the grains fall back from the passive zone  
 427 toward the edge of the footing and form a loop-like resultant velocity profile. The spatial nature of the vortex is  
 428 consistent with Murthy et al. [22] where the sand medium was dense. The present study confirms the presence of  
 429 such vortex maps in loose and medium-dense sand as well.



430  
 431 **Fig. 11** Vortex formation of resultant velocity vectors for footing ( $B=38$ ) interacting with dense sand. Enlarged  
 432 view of the corner of the footing is also presented here

433 Computational studies based on finite element method, for example Griffiths et al. [52] and Kumar and Kouzer  
434 [38] have reported velocity discontinuities near the footing edge, but the current study has shown their evolution  
435 in the sand packing using PIV experiments. The presence of such vortices around the corner at  $q > q_{ult}$  is likely to  
436 be related to the local density at the corner rather than the bulk density underneath the footing. Hence, even in a  
437 loose sand under compression loading, once the materials close to the footing corner compact to a certain density  
438 that is close to the maximum density of the tested soil then vortex will be observed around the edge of the footing.  
439 Since features like this are really local features and not bulk features, so it is the density in the local zone around  
440 the corner that would be important than the whole soil density for characterise of the vortex formation.

441 Figure 12 quantifies the normalised vertical displacement component  $S_v$  and horizontal displacement component  
442  $S_h$  of dense sand (for a typical case of  $B=38\text{mm}$ ) at different loading levels ( $q \leq q_{ult}$ ). These plots for loose and  
443 medium-dense sand are provided in the Online Resource OR9.  $S_v$  presents an inverted triangle-like profile that  
444 becomes deeper and narrower with increasing load level. The maximum value of  $S_v$  occurs along the footing  
445 centre, then decreases gradually towards the footing edge [17].  $S_v$  decreases to zero within a distance of  $0.25B$   
446 from the footing edge. This behaviour is due to the lack of confinement in the soil [11]. The secondary peaks in  
447 the distribution of  $S_v$  diminish with decrease in the density of sand. Such patterns, at times non-symmetric, are  
448 seen mostly at or beyond the ultimate load even under the symmetric loading conditions on the footing as  
449 discussed earlier. The secondary peaks increase with increasing density as shown in Online Resource OR9. This  
450 could be due to the particles interlocking, jamming and dilation that increase with the relative density of sand.



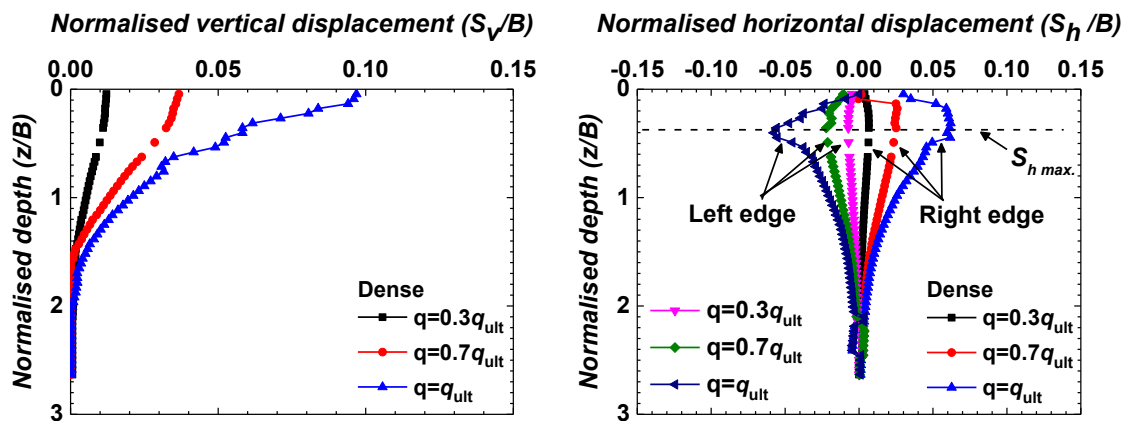
451  
452 **Fig. 12** For a typical case of dense sand: (left) Normalised vertical displacement component (right) normalised  
453 horizontal displacement component at a horizontal cross section  $0.5B$  below footing using PIV at different loading  
454 levels. Signs: vertical displacement (positive down, negative up), horizontal displacement (Negative toward left,  
455 positive toward right from the central axis).  $B = 38\text{ mm}$

456

457 The profile of  $S_h$  component presents S-like shape with a neutral point (zero value) occurring along the axis of  
 458 symmetry of the footing. The soil along the vertical axis of symmetry is confined by the maximum vertical  
 459 displacement and therefore  $S_h \sim 0$ . It is worth mentioning that, though not presented here, the variation of resultant  
 460 displacement ( $S_R = \sqrt{S_v^2 + S_h^2}$ ) at the footing-soil interface was uniform along the footing width.

461

462 Previous classical approaches have estimated the elastic settlement of footings using influence factors, which  
 463 could vary along the depth of sand [8, 53]. Such variations are also observed from numerical solutions, for  
 464 example using finite element method [53], elastic theory [16] and simple triangular profile using in situ cone  
 465 penetration tests [14]. However, they show different types of profiles. Using PIV here, the variation of  $S_v/B$  along  
 466 the centre line of the footing is examined, and  $S_h/B$  along the edge of the footing with depth for a typical case of  
 467 dense sand ( $B=38$  mm) is presented in Figure 13. These results for the cases of loose and medium-dense sand are  
 468 provided in the Online Resource OR10.



469

470 **Fig. 13** Settlement profiles with depth  $z$  from the bottom surface of the footing at different loading levels for a  
 471 typical case of dense sand: (left) normalised vertical displacement component (right) normalised horizontal  
 472 displacement for the sand packing.  $B=38$  mm

473

474 They show a nonlinear response for all cases of sand packing. They gradually decrease to a negligible value  
 475 beyond  $\sim z/B=2.5$ , similar results have been reported for loose sand by Liu and Iskander [17], however this  
 476 distance decreases for an increase in the relative density of sand. The normalised vertical displacement ( $S_v/B$ )  
 477 attains the peak at a depth of about  $0.1B$  for all cases of sand packing and footing widths, which are almost  
 478 independent of the loading stages.

479 Similarly, the normalised horizontal displacement component ( $S_h/B$ ) attains maximum at a depth of about  $0.25B$   
480 from the surface of the footing. At  $q \leq q_{ult}$ , the maximum value of normalised vertical displacement for smaller  
481 width ( $B=38\text{mm}$ ) is:  $S_{v\ max}/B=0.070, 0.086$  and  $0.096$  and  $S_{h\ max}/B= 0.02, 0.03$  and  $0.07$  for loose, medium-dense  
482 and dense sand respectively. These values increase with the relative density and load level. But, these values for  
483 the larger width of footing ( $B=76\ \text{mm}$ ) is:  $S_{v\ max}/B=0.045, 0.052$  and  $0.074$  for loose, medium-dense and dense  
484 sand respectively. The authors observed that the values of  $S_{v\ max}/B$  at ultimate load are close to the measured values  
485 of  $S_v/B$  presented earlier. Interestingly, the values of  $S_{v\ max}/B$  agree with the common assumption of using  $S/B$   
486 between  $0.05B - 0.1B$  for estimating  $q_{ult}$  from the load-settlement plots in foundation engineering designs [25, 36,  
487 53]. Overall, the displacement measures reported here could be used to derive more realistic description of  
488 displacement profiles in soil media in future.

## 489 **Conclusions**

490  
491 PIV is shown to be effective and promising in understanding the local and global geomechanical characteristics  
492 of footing interacting with sand media of different relative densities in a coherent manner. Where possible, the  
493 displacement measures and generic characteristics of velocity fields in the sand are compared with existing  
494 literature and FEM analysis and a good level of agreement is obtained. PIV clearly shows detailed descriptions  
495 of the stages of velocity discontinuities for the sand media. The velocity profiles of the medium-dense and dense  
496 sand are consistent with Vesic [43] but the advanced measurements reported here detect their evolutions more  
497 precisely. For the loose sand, the velocity discontinuities could reach the free surface. Significant vortex zones  
498 are existent near the footing corner at and beyond the ultimate bearing capacity of sand of all relative densities  
499 studied here. The boundaries of the zone of plastic flow in sand at failure load profiled using the advanced PIV  
500 here are remarkably similar to such intuitive diagrams suggested by the forefathers of soil mechanics, for example  
501 Fröhlich in the 1930's and Terzaghi's in 1940's [48]. The depth at which the settlement vanishes in the sand  
502 decreases for increase in the relative density of sand. The present study provides both the spatial and temporal  
503 distribution of displacements in soils of different packing densities under key stages of loading elegantly. PIV  
504 could be applied in future to develop robust failure surfaces for more complex soil profiles and foundation types  
505 encountered in geotechnical engineering applications. Further analysis is required for evaluating the scaling and  
506 size effects of footing-sand interactions in a detailed manner with a better resolution of the digital measurements  
507 (e.g. using multiple grids per grain). Also simulations using discrete element method (DEM) could be more  
508 suitable to model the grain-scale movements of granular assemblies under mechanical loading, but they would

509 require extensive level of computing resources to study the cases considered in this work. However, as shown in  
510 the current manuscript, FEM-based displacement fields can match to the level of local-scale grain displacements  
511 of corresponding experimental systems based on PIV. In particular, experiments-based, user-defined constitutive  
512 relation was used as input in the FEM simulations here which is found to be useful. Studies are underway in our  
513 group to extend the present research strategy to account for more complex conditions and realistic sand profiles  
514 in footing-sand interactions – for example layered soil systems, interference effects and roughness effects of  
515 footings.

516

## 517 **References**

518

- 519 1. Jaeger HM, Nagel SR, Behringer RP (1996) Granular solids, liquids, and gases. *Rev Mod Phys* 68(4):  
520 1259
- 521 2. Duran J (2000) *Sands, Powders and Grains*. Springer-Verlag, New York, USA
- 522 3. Desrues J, Viggiani G (2004) Strain localization in sand: an overview of the experimental results obtained  
523 in Grenoble using stereo photogrammetry. *Int J Num Analy Meth Geomech* 28(4): 279-321
- 524 4. Antony SJ (2007) Link between single-particle properties and macroscopic properties in particulate  
525 assemblies: role of structures within structures. *Phil Tran Roy Soc A: Math, Phy Eng Sci* 365(1861):  
526 2879-2891
- 527 5. Radjai F, Wolf DE, Jean M, Moreau J-J (1998) Bimodal character of stress transmission in granular  
528 packings. *Phys Rev letters*, 80(1): 61
- 529 6. Thornton C, Antony SJ (1998) Quasi-static deformation of particulate media. *Philo Trans Roy Soc A:*  
530 *Mathem Phys Eng Sci* 356:2763-2782
- 531 7. Kruyt N, Antony SJ (2007) Force, relative-displacement, and work networks in granular materials  
532 subjected to quasistatic deformation. *Phys Rev E* 75(5):051308
- 533 8. Bowles JE (1997) *Foundation Analysis and Design*. 5th ed., McGraw-Hill, Singapore
- 534 9. Liu C, Evett JB (2004) *Soils and foundations*. 6th ed Pearson Prentice Hall, New Jersey, USA
- 535 10. Fang H-Y (1991) *Foundation Engineering Handbook*. 2nd Chapman and Hall, New York, USA
- 536 11. Das BM (2009) *Shallow foundations: bearing capacity and settlement*. 2nd ed., CRC Press, London, UK
- 537 12. Terzaghi K, Peck RB (1967) *Soil mechanics in engineering practice*. Wiley, London, UK
- 538 13. Hansbo S (1994) *Foundation engineering*. Elsevier, London, UK

- 539 14. Schmertmann JH, Brown PR, Hartman JP (1978) Improved strain influence factor diagrams. *J Geotech*  
540 *Eng Div, Proc ASCE* 104(8):1131-1135
- 541 15. Powrie W (2014) *Soil mechanics: concepts and applications*. 3rd ed., CRC Press, London, UK
- 542 16. Mayne PW, Poulos HG (1999) Approximate displacement influence factors for elastic shallow  
543 foundations. *J Geotech Geoenviron Eng* 125(6): 453-460
- 544 17. Liu J, Iskander M (2004) Adaptive cross correlation for imaging displacements in soils. *J compu civ Eng*  
545 18(1): 46-57
- 546 18. Dynamic Studio (2013) *Dynamic Studio User's Guide*. Dantec Dynamics, Skovlunde, Denmark
- 547 19. Albaraki S, Antony SJ (2014) How does internal angle of hoppers affect granular flow? *Experimental*  
548 *studies using Digital Particle Image Velocimetry*. *Powd Tech* 268:253-260
- 549 20. Adrian RJ (1991) Particle-imaging techniques for experimental fluid mechanics. *Ann Rev Fluid Mech*  
550 23(1): 261-304
- 551 21. Hamm E, Tapia F, Melo F (2011) Dynamics of shear bands in a dense granular material forced by a  
552 slowly moving rigid body. *Phys Rev E* 84(4): 041304
- 553 22. Murthy TG, Gnanamanickam E, Chandrasekar S (2012) Deformation field in indentation of a granular  
554 ensemble. *Phys Rev E* 85(6): 061306
- 555 23. Cheng Y, White DJ, Bowman ET, Bolton MD, Soga K (2001) The observation of soil microstructure  
556 under load. *Powd Grains 2001*. Balkema: 69-72
- 557 24. White D, Take W, Bolton M (2003) Soil deformation measurement using particle image velocimetry  
558 (PIV) and photogrammetry. *Geotech* 53(7):619-631
- 559 25. O'Loughlin C, Lehane B (2010) Nonlinear cone penetration test-based method for predicting footing  
560 settlements on sand. *J Geotech Geoenviron Eng* 136(3): 409-416
- 561 26. Jahanger ZK, Antony SJ, Richter J (2016) Displacement patterns beneath a rigid beam indenting on  
562 layered soil. *Pro. Eighth Amer. Reg. Conf. Inter. Soc. Terrain-Vehicle Sys. Michigan, USA, Paper No.67*
- 563 27. ASTM Standard (1989) *Soil and Rock, Building, Stores, Geotextiles*. 04.08, West Conshohocken, Pa,  
564 USA
- 565 28. Head K (2006) *Manual of Soil Laboratory Test. Volume 1: soil Classification and Compaction Tests*.  
566 3rd ed CRC Press, Boca Raton, FL, USA
- 567 29. Dijkstra J, White DJ, Gaudin C (2013) Comparison of failure modes below footings on carbonate and  
568 silica sands. *Int J Phys Model Geotech* 13(1):1-12

- 569 30. White D, Bolton M (2004) Displacement and strain paths during plane-strain model pile installation in  
570 sand. *Géotech* 54(6):375-397
- 571 31. Cerato AB, Lutenege AJ (2007) Scale effects of shallow foundation bearing capacity on granular  
572 material. *J Geo Geoen Eng* 133(10): 1192-1202
- 573 32. Altaee A, Fellenius BH (1994) Physical modeling in sand. *Can Geotech J* 31(3): 420-431
- 574 33. Lau CK (1988) Scale effects in tests on footings. PhD thesis, University of Cambridge, UK
- 575 34. Raymond GP, Komos FE (1978) Repeated load testing of a model plane strain footing. *Can Geotech J*  
576 15(2): 190-201
- 577 35. Das BM (2011) Principles of foundation engineering. 7th ed., Global engineering, Connecticut USA
- 578 36. Kumar J, Bhoi MK (2009) Interference of two closely spaced strip footings on sand using model tests. *J*  
579 *Geotech Geoenviron Eng* 135(4):595-604
- 580 37. ANSYS 17.2 (2016) ANSYS Theory Manual. ANSYS, Inc., Canonsburg, Pennsylvania, USA
- 581 38. Kumar J, Kouzer K (2007) Effect of footing roughness on bearing capacity factor  $N_{\gamma}$ . *J Geotech*  
582 *Geoenvironl Eng* 133(5): 502-511
- 583 39. Mosadegh A, Nikraz H (2015) Bearing Capacity Evaluation of Footing on a Layered-Soil using  
584 ABAQUS. *J Earth Sci Clima Chan* 6(3):264
- 585 40. Gordan B, Adnan A, Aida MA (2014) Soil saturated simulation in embankment during strong earthquake  
586 by effect of elasticity modulus. *Model Simul Eng* 2014:20
- 587 41. Lee H-H (2015) Finite element simulations with ANSYS workbench 16. SDC publications, USA
- 588 42. Akbas SO, Kulhawy FH (2009) Axial compression of footings in cohesionless soils. I: Load-settlement  
589 behavior. *J Geotech Geoen Eng* 135(11):1562-1574
- 590 43. Vesic AS (1973) Analysis of ultimate loads of shallow foundations. *J Soil Mech Found Divis ASCE*,  
591 99(SM1):45-73
- 592 44. De Beer EE (1965) Bearing capacity and settlement of shallow foundations on sand. *Proc Sympo Bear*  
593 *Capac Settl Found Duke University, Durham, N.C.:* 15-33
- 594 45. Jewell RA (1989) Direct shear tests on sand. *Geotech* 39(2): 309-322
- 595 46. Lechinsky D, Marcozzi GF (1990) Bearing capacity of shallow foundations: rigid versus flexible  
596 models. *J Geotech Eng* 116(11):1750-175
- 597 47. Selvadurai APS (1979) Elastic Analysis of Soil-Foundation Interaction. *Dev. Geotech. Eng.*, 17,  
598 Elsevier Sci., Amsterdam, The Netherlands

- 599 48. Terzaghi K (1943) Theoretical soil mechanics. John Wiley and Sons Inc., New York, USA
- 600 49. Prandtl L (1920) "Über die härte plastischer körper [On the hardness of plastic bodies]. Math Phys Kl:
- 601 74-85
- 602 50. Bolton M (1986) The strength and dilatancy of sands. Geotech 36(1): 65-78
- 603 51. Lutenecker AJ, DeGroot DJ (1995) Settlement of shallow foundations on granular soils. Report no.
- 604 6332, University of Massachusetts Transportation Centre, USA
- 605 52. Griffiths DV, Fenton GA, Manoharan N (2006) Undrained bearing capacity of two-strip footings on
- 606 spatially random soil. Int J Geomech 6(6):421-427
- 607 53. Lee J, Eun J, Prezzi M, Salgado R (2008) Strain influence diagrams for settlement estimation of both
- 608 isolated and multiple footings in sand. J Geotech Geoenviron Eng 134(4): 417-427

609 **Figure Captions**

610 **Fig. 1** (a) Experimental setup using PIV with a live image of footing in contact with sand (b) schematic diagram

611 of the experimental setup (dimensions are in mm)

612

613 **Fig. 2** CPT data for the sand packing

614 **Fig. 3** (left) Chosen domain and boundary conditions, half of domain analysis not to scale (right) finite element

615 mesh, and element enlarged.  $S_v$  is vertical displacement component and  $S_h$  is horizontal displacement component.

616  $B$  is the footing width

617

618 **Fig. 4** Load-settlement curves of footing ( $B=38\text{mm}$ ) interacting with loose, medium-dense and dense sand. The

619 guide arrows show the ultimate load level ( $P_{ult}$ ) of the sand packing

620

621 **Fig. 5** Comparison of PIV-based vertical displacement profile in dense sand at ultimate load below the footing

622 with FEM analysis (identical colour codes are used): (a) vertical displacement component (b) horizontal

623 displacement component below the footing. Taking advantage of FEM, the strain distributions are presented: (c)

624 normal and (d) shear elastic strain

625 **Fig. 6** (a) Resultant velocity vectors at a typical load of  $q=q_{ult}$  in loose sand and the scalar contours of the vertical

626 velocity using PIV (b) vertical strain rate  $\dot{\epsilon}_v$  (c) horizontal strain rate  $\dot{\epsilon}_h$ . Zones: 1- dead zone, 2-active zone, 3-

627 passive zone.  $B= 38 \text{ mm}$

628

629 **Fig. 7** (a) Resultant velocity vectors at a typical load of  $q=q_{ult}$  in medium-dense sand and the scalar contours of

630 the vertical velocity using PIV (b) vertical strain rate  $\dot{\epsilon}_v$  (c) horizontal strain rate  $\dot{\epsilon}_h$ . Zones: 1- dead zone, 2-

631 active zone, 3- passive zone.  $B= 38 \text{ mm}$

632

633 **Fig. 8** (a) Resultant velocity vectors at a typical load of  $q=q_{ult}$  in dense sand and the scalar contours of the

634 vertical velocity using PIV (b) vertical strain rate  $\dot{\epsilon}_v$  (c) horizontal strain rate  $\dot{\epsilon}_h$ . Zones: 1- dead zone, 2-active

635 zone, 3- passive zone.  $B= 38 \text{ mm}$

636

637 **Fig. 9** (left) Resultant velocity vectors of soil movement under ultimate bearing capacity,  $B=38$  mm (right) sketch  
638 of general schematic failure mechanism underneath footing of different packing densities

639

640 **Fig. 10** PIV-based normalised vertical displacement component profiles in dense sand under the ultimate load  
641 ( $q=q_{ult}$ ) along different horizontal sections at different depths ( $z/B$ ) from the footing-soil interface

642

643 **Fig. 11** Vortex formation of resultant velocity vectors for footing ( $B=38$ ) interacting with dense sand. Enlarged  
644 view of the corner of the footing is also presented here

645

646 **Fig. 12** For a typical case of dense sand: (left) Normalised vertical displacement component (right) normalised  
647 horizontal displacement component at a horizontal cross section  $0.5B$  below footing using PIV at different loading  
648 levels. Signs: vertical displacement (positive down, negative up), horizontal displacement (Negative toward left,  
649 positive toward right from the central axis).  $B = 38$  mm

650

651 **Fig. 13** Settlement profiles with depth  $z$  from the bottom surface of the footing at different loading levels for a  
652 typical case of dense sand: (left) normalised vertical displacement component (right) normalised horizontal  
653 displacement for the sand packing.  $B= 38$  mm

**Table 1.** Experimentally measured physical properties of the sand used

Type of sand	Loose (L)	Medium-dense (M)	Dense (D)	Standards
Dry density ( $\gamma_d$ ): (kN/m <sup>3</sup> )	14.70	15.30	15.80	ASTM C29/C29M
Void ratio ( $e_o$ )	0.76	0.70	0.64	
Relative density, $D_r$ : %	24	53	72	ASTM C128
Peak angle of internal friction, $\phi_{peak}$ : °	32(32.4)*	39(39.5)*	44.3(46.1)*	
Residual angle of internal friction, $\phi_{cr}$ : °	30	32	36.3	ASTM D3080
Maximum dry density ( $\gamma_{dmax}$ ): kN/m <sup>3</sup>		16.50		ASTM D698
Minimum dry density ( $\gamma_{dmin}$ ): kN/m <sup>3</sup>		14.23		ASTM D4254 method C
Maximum void ratio ( $e_{max}$ )		0.83		ASTM C29/C29M
Minimum void ratio ( $e_{min}$ )		0.58		ASTM C29/C29M
$D_{10}$ : mm		0.25		
$D_{30}$ : mm		0.31		ASTM D421
$D_{50}$ : mm		0.37		ASTM D422
$D_{60}$ : mm		0.40		
Uniformity coefficient, $C_U$		1.55		
Coefficient of curvature, $C_C$		0.93		ASTM D2487
Mineralogy		Silica		
Grain shape		Mostly spherical to sub-prismoidal		Head (2006)
Angularity of grains		Angular and sub angular		
Angle of repose of the sand		34°		Head (2006)

()\* Direct shear test results